Influence of Wall Proximity on the Lift and Drag of a Particle in an Oscillatory Flow

Paul F. Fischer,[1] Gary K. Leaf,[1] and Juan M. Restrepo*[2]

[1] *Mathematics and Computer Science Division, Argonne National Laboratory*

Argonne, IL 60439, U.S.A.

[2] *Department of Mathematics and Department of Physics*

University of Arizona, Tucson, AZ 85721, U.S.A.

**Corresponding Author:.* `restrepo@math.arizona.edu`, TEL: (520) 621-4367, FAX (520) 621-8322.

Abstract

We report on the lift and drag forces on a stationary sphere subjected to a wall-bounded oscillatory flow. We show how these forces depend on two parameters, namely, the distance between the particle and the bounding wall, and on the frequency of the oscillatory flow. The forces were obtained from numerical solutions of the unsteady incompressible Navier-Stokes equations.

For the range of parameters considered, a spectral analysis found that the forces depended on a small number of degrees of freedom. The drag force manifested little change in character as the parameters varied. On the other hand, the lift force varied significantly: we found that the lift force can have a positive as well as a negative time-averaged value, with an intermediate range of external forcing periods in which enhanced positive lift is possible. Furthermore, we determined that this force exhibits a viscous-dominated and a pressure-dominated range of parameters.

Keywords: lift, drag, sphere, wall-bounded flow, oscillatory flow.

1 Introduction

We study the lift and drag forces on a sphere that is held a fixed distance away from an ideally smooth wall. The sphere is immersed in an incompressible fluid that is subjected to time-periodic forcing. This study is a follow-up on Fischer, Leaf & Restrepo (2002) (hereafter referred to as FLR02), in which we explored the dependence of the lift and drag on the Reynolds number and the nondimensional forcing period, referred to as the Keulegan-Carpenter number. In that study the sphere was also held fixed in time and space; however, it rested on the bounding wall. The methodology followed here is the same as in FLR02: we use time-dependent three-dimensional simulations of the Navier-Stokes equations to obtain the flow from which we can obtain the lift and drag on the particle.

In FLR02, we reported that, for the range of parameters considered, the lift and drag varied more dramatically with changes in the Keulegan-Carpenter number rather than with changes in the Reynolds number. In this study we focus on how these forces depend on the Keulegan-Carpenter number and on the *gap*, which is the shortest distance between the surface of the sphere and the wall, normalized to the diameter of the particle.

Numerous studies have examined oscillatory flows past stationary cylinders (e.g., Bearman, Downie, Graham & Obasaju (1985); Sarpkaya (1986); Obasaju, Bearman & Graham (1988); Justesen (1991)). Many of these studies have been motivated primarily by the need to characterize forces resulting from rhythmic flow around submerged pipes in oceanic settings. Little, however, has appeared in print regarding forces on a spherical particle in an oscillating flow, particularly in proximity to a bounding wall.

When one compares the experimental results of Rosenthal & Sleath (1986) and FLR02, it becomes clear that the topological differences between two-dimensional cylinder flow and three-dimensional flow past a sphere prevent one from extrapolating the cylinder results to the spherical case.

Our flow configuration is characterized by the three independent flow parameters: the Keulegan-Carpenter number, the Reynolds number, and the gap. The resulting fluid motion due to an oscillating far-field velocity field is unsteady, and thus steady-state or unidirectional analyses are not generally applicable. Hence, the Keulegan-Carpenter number plays a more prominent role in determining the nature of the flow than does the Reynolds number. Indeed, this was borne out in FLR02: variations in the flow were significantly more dramatic when the Keulegan-Carpenter number was varied, rather than when the Reynolds number was varied, when the particle was resting on the bounding wall. Our present calculations do not indicate that introducing a gap changes this outcome much. Hence, all results presented here correspond to a fixed Reynolds number of 100. The insensitivity of the lift and drag to the Reynolds number is not totally unexpected: the Reynolds number is defined in terms of the the maximum speed of the far-field (bulk) flow, the diameter of the particle, and the fluid viscosity. This choice of Reynolds number is more appropriate for a steady-flow situation; nevertheless, we use it because FLR02 as well as this study were inspired by experimental work due to Rosenthal & Sleath (1986) in which the Reynolds number was defined as stated above. The gap parameter, on the other hand, is particularly important because the proximity of a wall to an object subjected to steady flows has a significant influence on the forces experienced by the particle (see Hall (1988); Cherukat, McLaughlin & Graham (1994); Asmolov &

McLaughlin (1999), and references mentioned in these works). It would be reasonable to expect important changes on the lift and drag forces on a particle subjected to a flow in the vicinity of a wall when the gap width is varied, especially if the boundary layers in the neighborhood of the wall and the sphere are comparable to the gap width.

In Section 2 we describe the physical configuration of the particle and the flow. We also briefly describe how this flow is computed numerically. In Section 3 we present the numerical results of measurements of the drag force and discuss its dependence on the gap and frequency parameters of the flow. In Section 4 we discuss the results for the lift force. In Section 5 we consider the dynamic implications of combined drag and lift forces. We also describe the qualitative changes that occur in the flow field and how they relate to changes on the lift and drag forces. A summary of the results appears in Section 6.

2 Computational Model

Our computational model is based on the incompressible Navier-Stokes equations, given in nondimensional form by

$$\frac{\partial \mathbf{u}}{\partial t} + \mathbf{u} \cdot \nabla \mathbf{u} = -\nabla p + \frac{1}{Re} \nabla^2 \mathbf{u}, \tag{1}$$

$$\nabla \cdot \mathbf{u} = 0, \tag{2}$$

where $\mathbf{u} = (u, v, w)$ is the nondimensional velocity and p is the pressure normalized by the fluid density ρ. The equations are nondimensionalized by the characteristic length-scale D, the particle diameter, and the convective time-scale, D/U, where U is the amplitude of oscillation in the far-field velocity.

The Reynolds number is $Re := UD/\nu$, with ν the kinematic viscosity. The results presented below have a fixed Reynolds number of $Re = 100$.

The discretization of (1) is based on the spectral element method in space and a characteristics-based second-order accurate splitting in time (Maday, Patera & Rønquist (1990)). Full details of the discretization can be found in FLR02 and Fischer (1997). The computational domain is the parallelepiped $[-L_x, L_x] \times [-L_y, 0] \times [0, L_z]$. Homogeneous Dirichlet conditions ($\mathbf{u} = \mathbf{0}$) are applied on the bounding wall, located at z=0, and on the surface of the unit-diameter sphere centered at $(x, y, z) = (0, 0, \frac{1}{2} + \epsilon)$. Here, ϵ is the nondimensional gap width, referenced to the diameter D of the sphere. Boundary conditions on the $y = -L_y$ and $z = L_z$ planes are free-slip, no-penetration, which correspond to reflection symmetry about the given plane. In order to reduce computational cost, symmetry conditions are also employed about the $y = 0$ plane. A full three-dimensional calculation carried out in FLR02 demonstrated the appropriateness of the bilateral symmetry assumption under the current flow conditions. Table 1 lists the domain sizes and number of elements, K, employed for each value of ϵ considered. All reported cases are run with polynomial degree $N = 5$ in each element. For all cases, the timestep size was Δt=.05, in convective time units. Note that it is the convective timescale that determines the stability and accuracy constraints on Δt and not the period τ. The CPU time per simulation period thus scales in direct proportion to τ.

Several mesh convergence studies with N=8 and N=10 confirmed mesh independence. The appropriateness of the timestep and domain sizes were also confirmed. For the particular case of $\epsilon = 1$, $\tau = 10$, the mean lift for a simulation with N=10, K=9632, Δt=.025, and domain dimensions

Table 1: Gap size, domain dimensions, and number of elements.

ϵ	L_x	L_y	L_z	K
0.0156	27.5	5.5	7.8156	2836
0.125	27.5	5.5	7.925	2836
0.25	28.0	9.0	10.50	4116
0.50	28.0	9.0	10.75	4116
0.70	28.0	9.0	11.00	4116
1.00	28.0	9.0	11.75	4116

(L_x, L_y, L_z) = (38,16,15) was found to be within 0.4 % of the production simulation run. The maximum difference in the lift coefficient was 0.9 % over a given period.

The base flow conditions are such that, in the absence of the particle, the nondimensionalized velocity field would be

$$\mathbf{u}_b = \left(\sin(\frac{2\pi t}{\tau}) - e^{-z/\delta}\sin(\frac{2\pi t}{\tau} - z/\delta), 0, 0\right), \tag{3}$$

which corresponds to a unit-amplitude velocity field oscillating back and forth in the x-direction with nondimensional period τ. For viscous flows, this results in a time-periodic boundary layer with characteristic thickness

$$\delta = \sqrt{\frac{\tau}{\pi Re}}.$$

In this study the period is in the range $10 \leq \tau \leq 300$, and thus the Stokes layer range is $0.17 < \delta < 0.98$, which is comparable to the range of the gap, $0.0156 \leq \epsilon \leq 1.0$.

As in FLR02, we use $\mathbf{u} = \mathbf{0}$ as an initial condition in all cases. The base flow is established in one of two ways, depending on the period. For

relatively short periods ($\tau \leq 40$), periodic boundary conditions are used in the x-direction, and the flow is forced by a time-periodic mean pressure gradient. Because (1) is linear in p, we can write the pressure as

$$p = p'(x, y, z, t) + p_0(x, t), \tag{4}$$

where

$$p_0 := \frac{2\pi x}{\tau} \cos\left(\frac{2\pi t}{\tau}\right) \tag{5}$$

supplies the desired time-dependent mean pressure gradient and p' is the computed perturbation pressure, which is spatially periodic. Note that drag-coefficient computations must include the full pressure (4) and not just the computed perturbation p'.

For longer periods, the base flow is established by specifying Dirichlet conditions on either end of the domain. When the far-field base flow is in the positive x direction, we set $\mathbf{u}(-L_x, y, z, t) = \mathbf{u}_b$ and use a homogeneous Neumann condition at $x = +L_x$. When the far-field base flow is in the negative x direction, we reverse these conditions. The Neumann condition corresponds to the usual outflow (natural) boundary condition associated with the Stokes subproblem that is solved in each step. Note that the required hydrostatic forcing results directly from application of the boundary conditions and that the auxiliary pressure p_0 is not needed.

We tested the consistency of the results with regard to changing boundary condition strategies. The maximum difference between the lift computed with the periodic boundary conditions and the inflow/outflow boundary conditions for $\tau = 40$ and $\epsilon = 0.5$ was 0.34 %.

At each time step, we compute the lift and drag coefficients, given by

$$C_L = \frac{F_z}{\frac{1}{2}A\rho U^2}, \tag{6}$$

$$C_D = \frac{F_x}{\frac{1}{2}A\rho U^2}, \tag{7}$$

respectively, where F_x and F_z are components of the dimensional force on the particle and $A = \pi D^2/4$ is the cross-sectional area. We introduce additional subscripts m, M, and A to indicate the respective minimum, maximum, and average of (6) and (7) over a single cycle in the time-periodic flow state.

3 Drag Calculations

The numerical simulations result in time histories of drag and lift data for each (τ, ϵ) pairing. A typical set of drag histories is shown in Figure 1 for the case of $\epsilon = 0.5$ and several values of τ. Figure 2 shows the constituent viscous and pressure contributions to the drag for the same cases. Over the range of parameters considered, the drag behavior is smooth and essentially monochromatic, with a dominant frequency of $f = 2\pi/\tau$. The pressure and viscous contributions are slightly out of phase for small τ. The phase lag becomes smaller as τ increases. These curves also show that only a few oscillations are required to obtain a periodic state, starting from rest, with a somewhat longer time frame for small τ. All of the summary data (minimum, maximum, and average) are computed during the final period.

In Figure 3, we plot $C_{D_M}(\epsilon, \tau)$, the peak drag coefficient, for each of the gap values considered. As $\tau \longrightarrow 0$, C_{D_M} exhibits a rapid increase and a similar value for all of the gaps considered. For the larger periods, there is a significant spread in the drag coefficient as a function of the gap, with larger

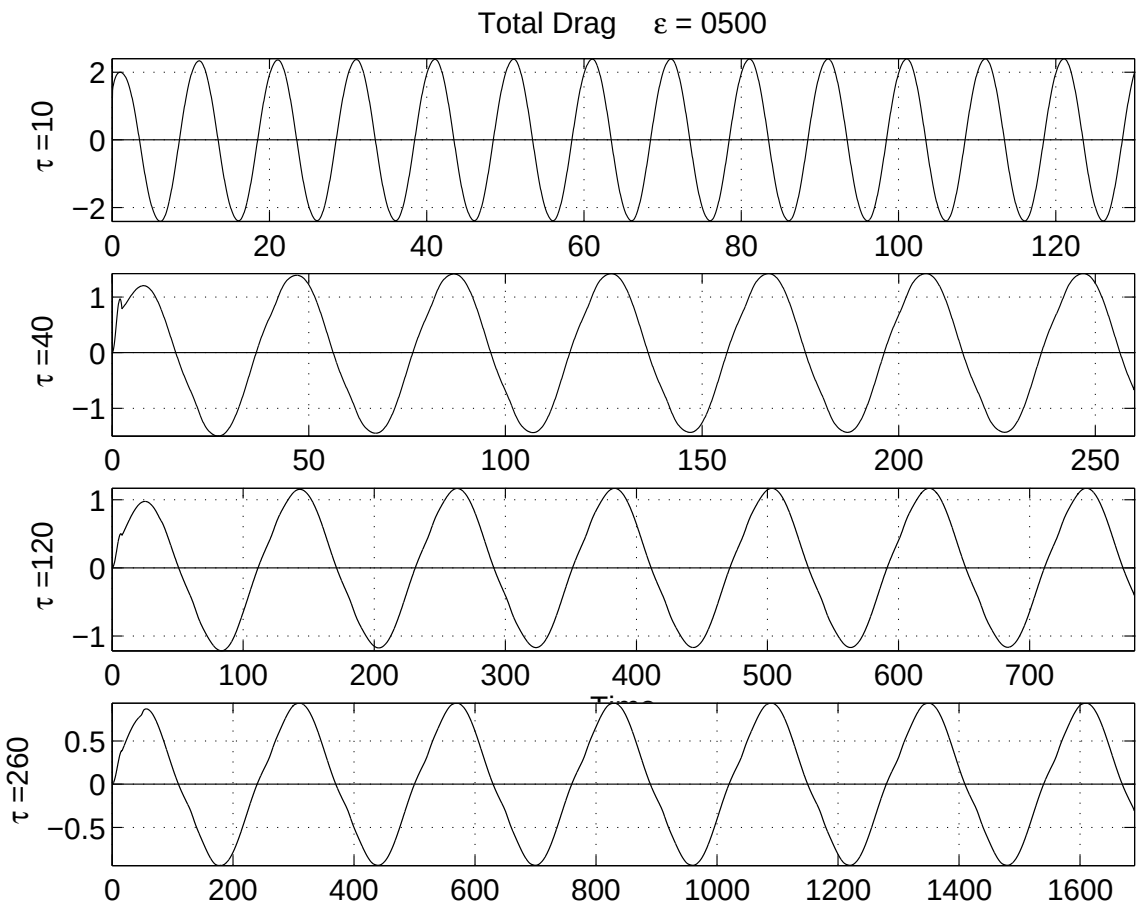

Figure 1: Drag histories for $\epsilon = 0.5$; (a) $\tau = 10$, (b) $\tau = 40$, (c) $\tau = 120$, and (d) $\tau = 260$.

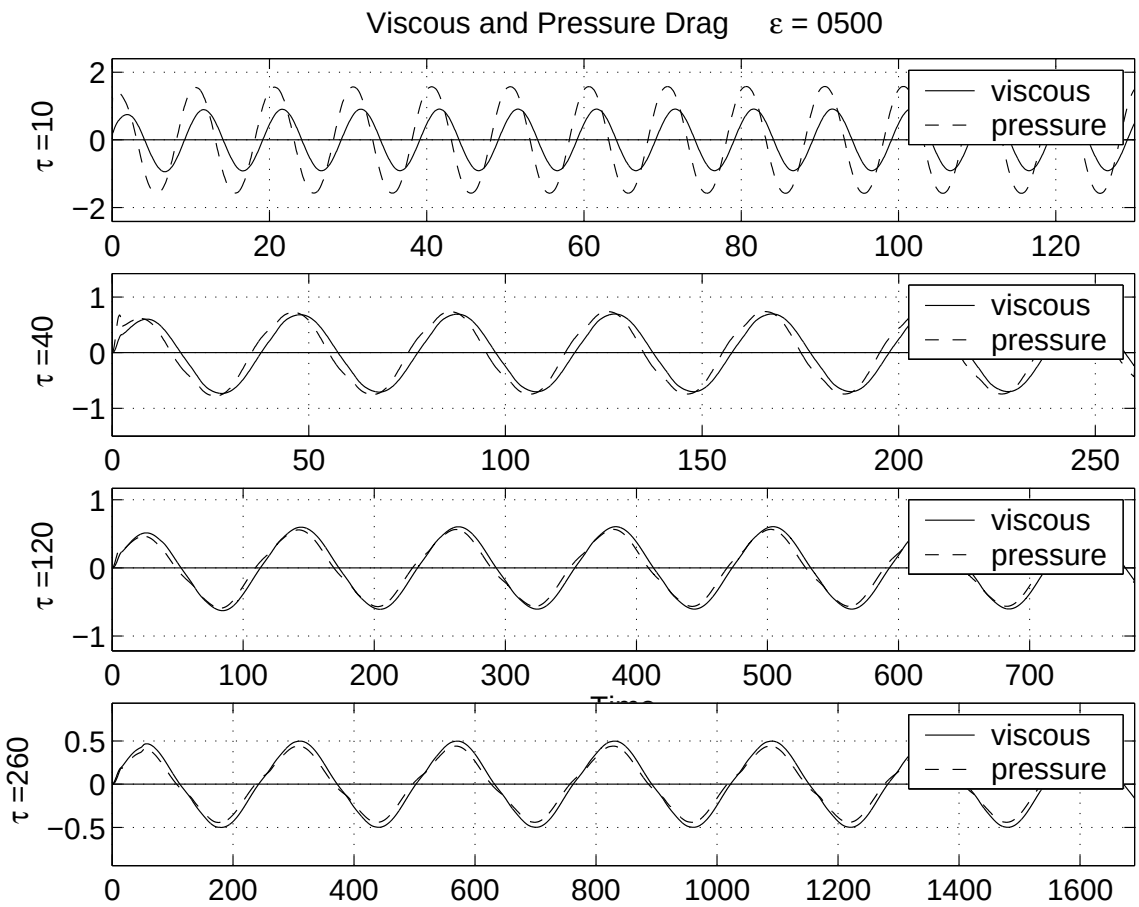

Figure 2: Pressure and viscous contributions to the drag histories for $\epsilon = 0.5$;

(a) $\tau = 10$, (b) $\tau = 40$, (c) $\tau = 120$, and (d) $\tau = 260$.

gaps corresponding to increased C_{D_M}.

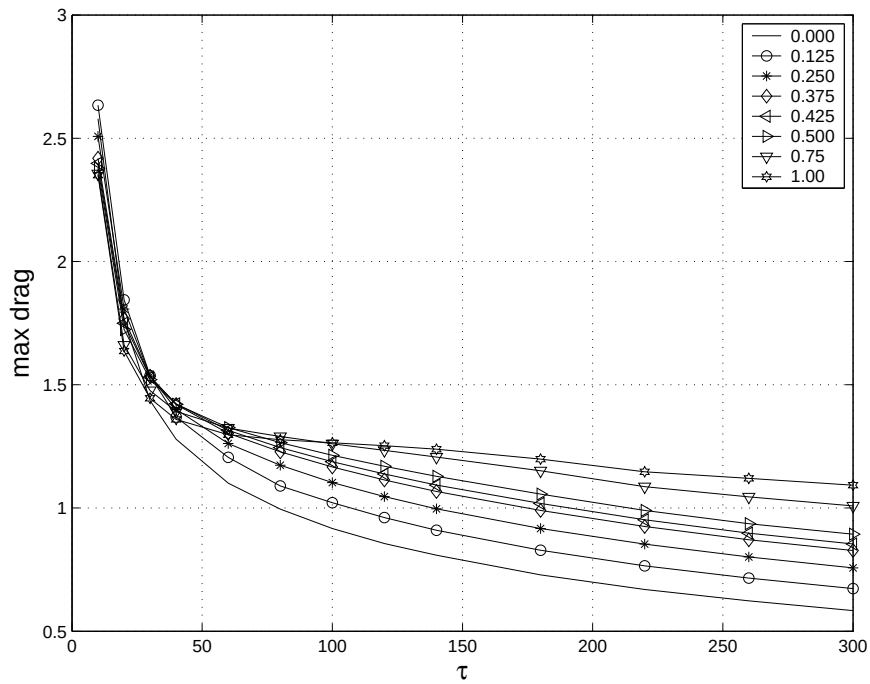

Figure 3: C_{D_M} as a function of gap ϵ and period τ.

The drag behavior can be understood by considering its constituent pressure and viscous components. The pressure drag consists of a term arising from the mean pressure gradient that drives the flow, $\frac{\partial p_0}{\partial x}$, and a term associated with the computed perturbation pressure p'. From (4) and (5), we see that the mean component scales as τ^{-1}, and we may expect this term to dominate the overall drag for sufficiently small periods. Because the mean pressure varies linearly with x, its contribution to drag is simply the pressure gradient times the volume of the particle. When normalized by $\frac{1}{2}\rho U^2$, the resulting contribution to C_{D_M} is

$$C_{D_{M,0}} = \frac{8\pi}{3}\frac{1}{\tau}. \tag{8}$$

While an inverse power-law trend is indicated by the data in Figure 3, the

exponent is not self evident. In Figure 4 we plot the C_{D_M} for $\epsilon = .125$, along with its respective pressure and viscous contributions, $C_{D_{M,p}}$ and $C_{D_{M,\nu}}$. (Note that C_{D_M} equals $C_{D_{M,p}} + C_{D_{M,\nu}}$ only when the pressure and viscous forces are in phase.) The slope of $C_{D_{M,p}}$ on this log-log scale indicates an exponent of about $-.63$ at $\tau = 10$, indicating that we are outside of the range where (8) is dominating the overall pressure. An extension to (8) is obtained by accounting for the flow-separation that results in additional pressure drag (the p' contribution). Supposing the flow is fully separated (i.e., $C_{D'} \approx 1$),

$$C_{D_p} \approx 1 \; + \; \frac{8\pi}{3}\frac{1}{\tau}, \tag{9}$$

which is also plotted in Figure 4.

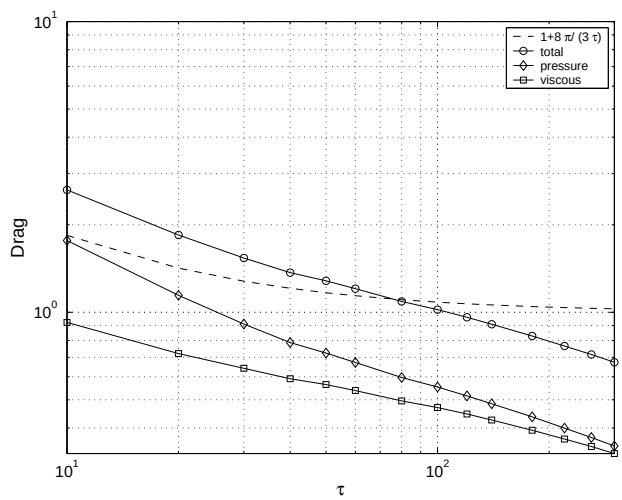

Figure 4: C_{D_M}, $C_{D_{M,p}}$, and $C_{D_{M,\nu}}$ for $\epsilon = 0.125$. Also plotted are Equations (8) and (9).

The magnitude of (9) is in reasonable agreement with $C_{D_{M,p}}$ for the smaller periods but is not correct for large τ, where (9)$\longrightarrow 1$, while $C_{D_{M,p}} \longrightarrow 0$ as τ increases. This result is to be expected, because the physics in the large-τ limit is quite different due to the interaction of the Stokes layer with

the particle. Figure 4 reveals that C_{D_M} drops substantially below unity for large τ. This drop is explained by the momentum deficit associated with the Stokes layer near the wall, which is growing as $\tau^{1/2}$. Particles within the Stokes layer do not "see" the full velocity magnitude, U. One might therefore expect that particles further from the wall would exhibit larger values of C_{D_M} in the large-τ limit. Conversely, for small τ and, hence, small δ, the drag behavior should not be strongly dependent on ϵ. These behaviors are indeed evident in Figure 3.

Regarding the viscous contribution to the drag, one can make arguments similar to that for the pressure in the case of short periods. The peak value of the viscous drag will scale as $\beta A \rho \nu U/\tilde{\delta}$, where A is the cross-sectional area, β an order-unity constant, and $\tilde{\delta}$ a characteristic boundary layer thickness on the particle surface. Standard dimensional arguments imply that the boundary layer thickness scales as $(\nu \tilde{t})^{1/2}$, where $\tilde{t}$ is a relevant viscous time scale. For long periods (neglecting any interaction with the Stokes layer), $\tilde{t}$ is essentially the time of flight for a fluid particle to pass the sphere, which is unity given our choice of nondimensionalization. For short periods, the time scale will be $\tilde{t} \approx \tau/2$, which is the length of time that the flow proceeds in a given direction. Thus, in the small-τ limit, we expect the viscous drag contribution to scale as $\tau^{-.5}$. In fact, we observe in Figure 4 $C_{D_{M,\nu}} \approx O(\tau^{-.4})$ for $\tau = 10$, which is in reasonable agreement with this analysis.

4 Lift Calculations

Figure 5 shows the lift histories for the $\epsilon = 0.5$ case at values of τ corresponding to the drag cases of Figure 1. Figure 6 shows the viscous and pressure

contributions to the lift for the same cases. We see that the time history of the lift does not exhibit the nearly simple harmonic behavior observed in the drag histories. For the shortest period, $\tau = 10$, the behavior is dominated by a single frequency, which is twice the fundamental frequency due to the fore-aft symmetry of the flow conditions. Nonetheless, the negative extrema are more sharply peaked than the positive extrema, thus indicating the presence of higher harmonics. In Figure 6 the contrasting sharpness of the peaks is clearly present in both the viscous and pressure lift contributions. For $\tau = 40$, a strong subharmonic at $\tau/4$ is present in both the viscous and pressure lift contributions. Finally, for $\tau = 260$, we return to a strong fundamental signal with period $\tau/2$. However, the viscous and pressure peaks are out of phase, such that the total lift is essentially a flat signal with periodic negative spikes. The negative extrema coincide with the change in sign of the bulk velocity field given by (3).

Figure 7 shows the maximum, minimum, and average lift as a function of ϵ and τ. By symmetry considerations, the lift is expected to go to zero as ϵ gets large. The figures clearly show this trend. We examined the $\epsilon = 4$ case (not shown in this paper) to confirm this outcome. We found that the lift becomes nearly simple-oscillatory with period $\tau/2$ and that its magnitude, for a fixed τ, is smaller than all other cases considered here, that is, tending to zero. In addition, the lift is expected to go to zero as τ goes to infinity. We return to this point in the subsequent discussion.

A salient feature of Figure 7 is the appearance of a regime of parameters that exhibit significant positive time-averaged lift, C_{L_A}, which we refer to as the transitional regime. The transitional range of parameter space ranges from roughly $\tau = 30$ to $\tau = 100$. The figure shows an increase in the average

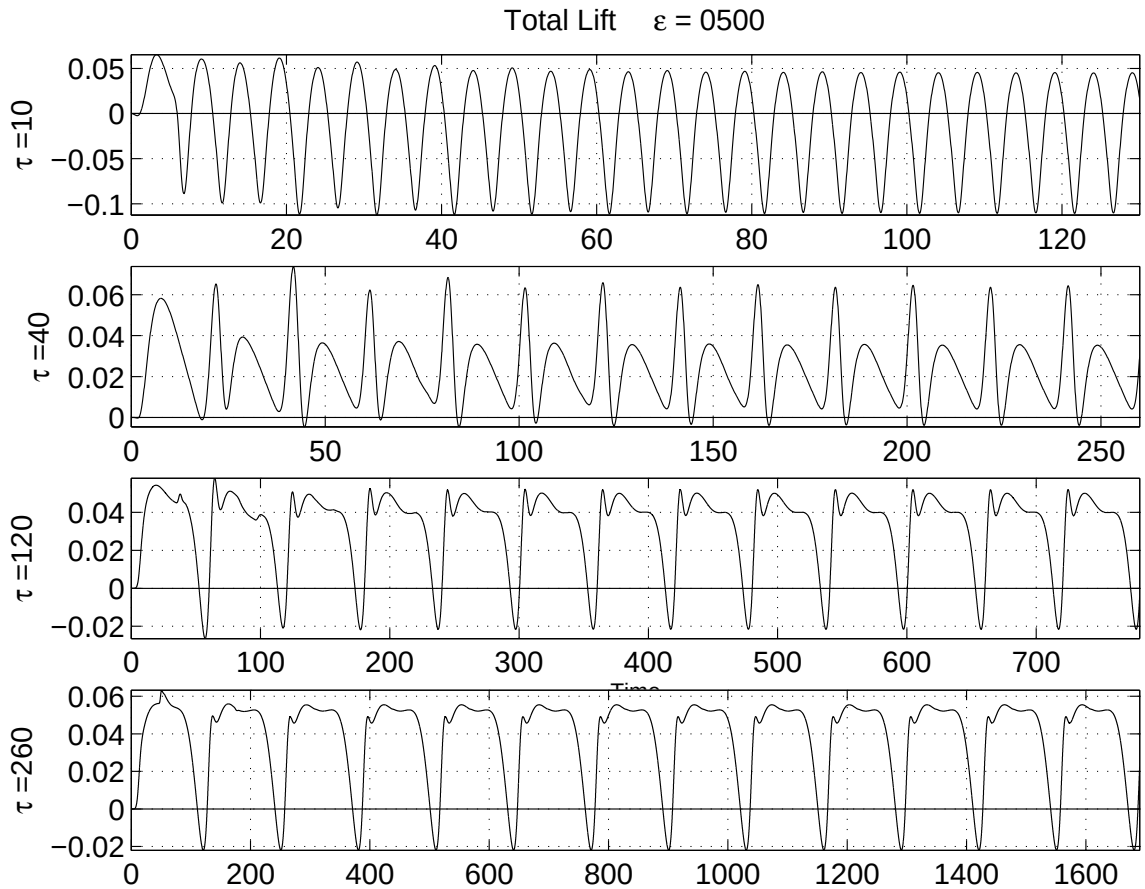

Figure 5: Lift histories for $\epsilon = 0.5$; (a) $\tau = 10$, (b) $\tau = 40$, (c) $\tau = 120$, and (d) $\tau = 260$.

lift in the transitional regime, particularly for small-gap cases. Below that transitional regime is one in which the average lift can be negative. That is, for a given gap width, there are values of τ small enough for which there is a net suction. On the other side of the transitional regime, C_{L_A} not change considerably with τ and represents a lift force that, on average, is directed away from the bounding wall. The $\epsilon = 0$ case has the most pronounced transitional region. Figure 7 shows that the maximum lift for $\epsilon = 0$ is positive for all $\tau > 10$. In FLR02, however, we found that the maximum quickly tends

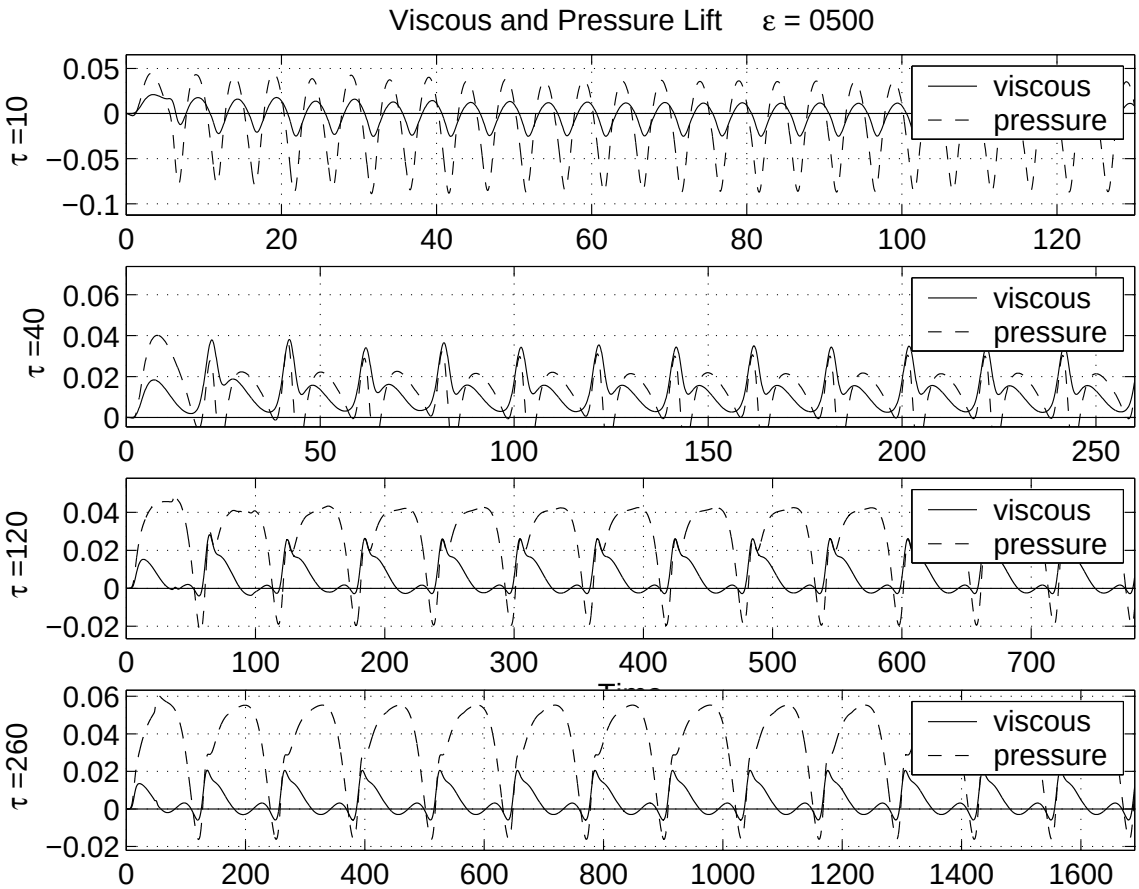

Figure 6: Pressure and viscous contributions to the lift histories for $\epsilon = 0.5$; (a) $\tau = 10$, (b) $\tau = 40$, (c) $\tau = 120$, and (d) $\tau = 260$.

to zero for values of $\tau < 10$. For the larger gap sizes investigated (i.e., for ϵ close to unity), the average lift is small and negative at $\tau = 10$.

Figure 8 shows the viscous and pressure components of the computed average lift as a function of ϵ and τ. These plots reveal viscous- and pressure-dominated lift regimes which are separated by a cross-over point in ϵ-τ space. For small gap widths, this crossover either does not occur or occurs for periods smaller than the ones examined in this study. In Figure 8a we see no crossover. In the remaining figures we see a crossover between the viscous

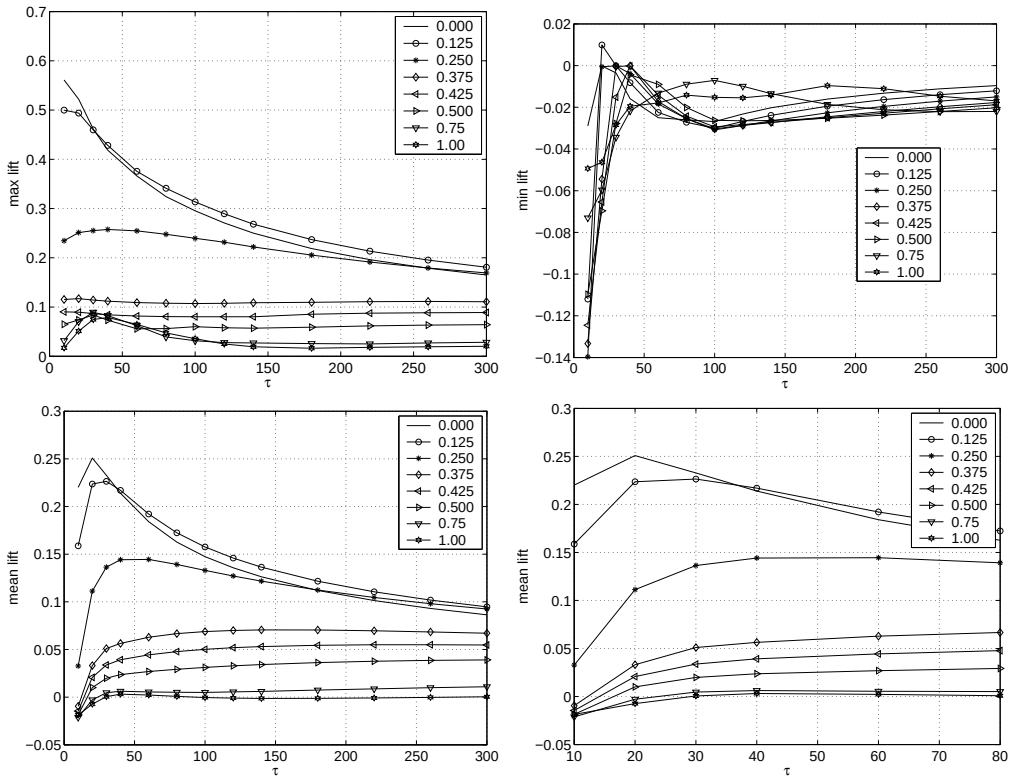

Figure 7: (a) C_{L_M}, (b) C_{L_m}, and (c)-(d) C_{L_A} as a function of gap ϵ and period τ; (d) shows small τ details of C_{L_A}.

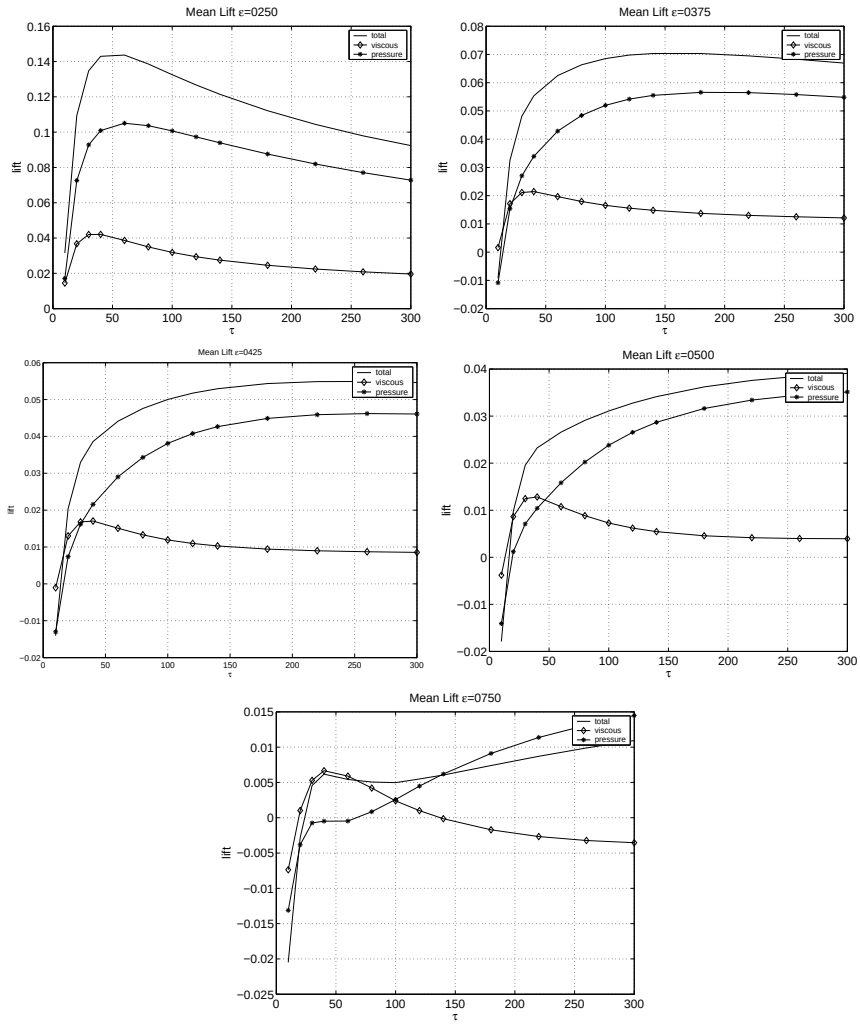

Figure 8: C_{L_A} (solid), average of the viscous component of the lift (diamonds), average of the pressure component of the lift (stars); as a function of τ, for (a) $\epsilon = 0.250$, (b) $\epsilon = 0.375$, (c) $\epsilon = 0.425$, (d) $\epsilon = 0.500$, and (e) $\epsilon = 0.750$. Note scales.

and pressure components. Furthermore, the crossover point clearly tends to larger values of τ as ϵ increases. Figure 9 shows the average lift regimes borne out of the numerical simulations. The crossover points were obtained numerically and were connected in the figure by straight lines. The average

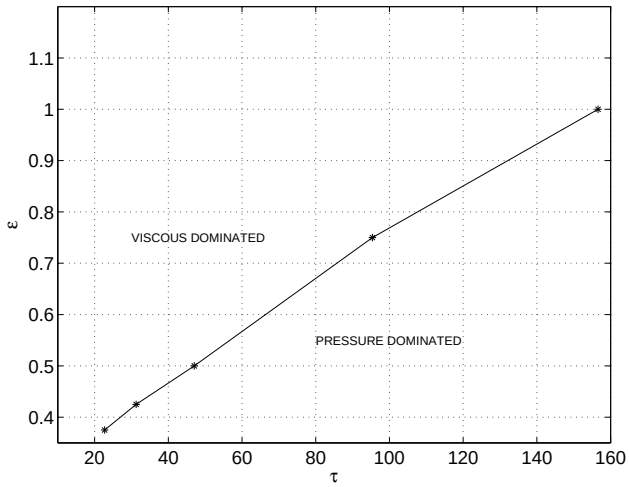

Figure 9: Boundary line in (ϵ, τ)-space for the pressure and the viscous dominated regimes for the average lift C_{L_A}. The calculated points have been connected by straight lines.

lift value at which crossover occurs becomes smaller in magnitude as both τ and ϵ get larger.

As mentioned, for fixed ϵ, the lift is expected to go to zero as τ goes to infinity. This would be the limit of Stokes flow.[1] Our computational configuration does not allow us to explore this limit, but the tendency is certainly present. It may be somewhat puzzling to consider the Stokes flow limit if we are holding the Reynolds number fixed at 100 in our exploration of parameter space. The apparent contradiction is resolved by realizing the Reynolds number used here, based on the external flow, becomes less relevant in the regime of very large τ: as τ goes to infinity the Stokes layer thickness gets larger (at a rate proportional to $\tau^{1/2}$); the Stokes layer becomes infinitely large, when compared to D, and the impinging velocity shear goes to zero.

[1]Not to be confused with Stokes boundary layer solution to oscillatory bounded flows.

To gain further insight to the nature of the lift force in the large-τ limit, we conducted a separate set of steady-state calculations. We considered the lift conditions in the large τ limit for the particular case $\epsilon = 0.5$. As $\tau \longrightarrow \infty$, we can expect the flow conditions to be quasi steady-state and $\delta \gg 1$. Under these conditions, the background velocity profile near the wall is $\mathbf{u} \approx (0, 0, cz)$. Here, c is found by differentiating (3),

$$c = \left.\frac{\partial u_b}{\partial z}\right|_{z=0} = \frac{1}{\delta}\left(\sin(2\pi t/\tau) + \cos(2\pi t/\tau)\right),$$

which takes as its maximum (over time)

$$c_{\max} = \frac{\sqrt{2}}{\delta} = \sqrt{\frac{2\pi Re}{\tau}}.$$

For $\epsilon = 0.5$, the center of the sphere is located at $z = 1$ and the velocity at the sphere center is thus $U^* := c$. The steady-state calculations used the same computational domain as considered in the oscillatory case but with boundary conditions such that the base flow corresponds to plane Couette

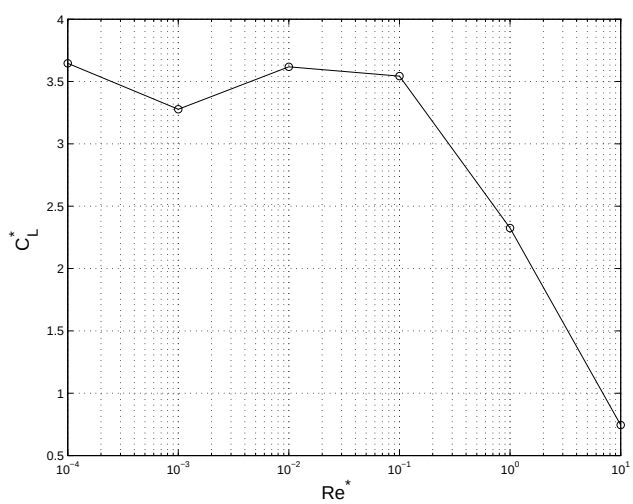

Figure 10: Lift for a sphere in a plane Couette flow, $\epsilon = 0.5$, for a $Re^* = DU^*/\nu$ in the range of $Re^* = 10^{-4}$–10^{1}.

flow with $\mathbf{u} \approx (0, 0, z)$ (i.e., the flow is normalized by the base-flow velocity U^*). We considered a series of trial runs with finite Reynolds numbers, $Re^* := DU^*/\nu$ in the range of $Re^* = 10^{-4}$–10^1. The computed lift coefficients are shown in Figure 10 and clearly show a trend toward an order unity constant. From the data,

$$C_L^* := \frac{L^*}{\frac{1}{2}\rho(U^*)^2} \approx 3.6.$$

The dimensional relationship between C_L^* and C_L is

$$C_L = \left(\frac{U^*}{U}\right)^2 C_L^* = \frac{2\pi Re}{\tau} C_L^*,$$

from which we conclude that

$$C_{L_M} \sim 3.6 \frac{2\pi Re}{\tau}$$

as $\tau \longrightarrow \infty$, for $\epsilon = 0.5$. For other values of ϵ we would expect a similar trend with a different order unity constant. Note that, for this limit to apply, we must have $\delta > 1 + \epsilon$ (the normalized sphere height), which implies $\tau \gg \pi Re(1 + \epsilon)^2$.

Figure 11 shows the spectral content of $C_L(t; \tau; \epsilon)$, corresponding to the cases considered in Figure 5. The most prominent feature of these plots is the relatively few degrees of freedom present in the lift signal, which suggests that a simple and practical parametrization of the lift might be possible. Regardless of the forcing period, the spectra will always contain the half-period signal (the lift goes through two cycles per forced oscillation). For short-period forcing, the spectra indicate that nearly all of the energy in the lift is captured by the $\tau/2$-period degree of freedom. As τ increases, a cascade of subharmonics appears. The overall energy of the signal also decreases (i.e.

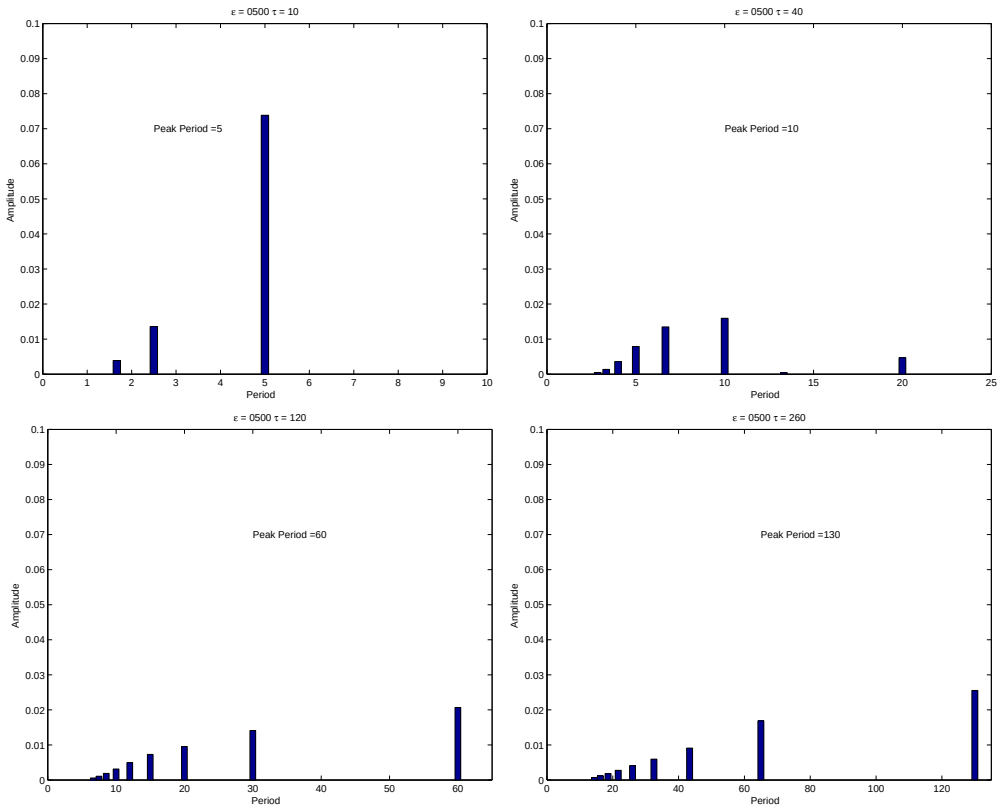

Figure 11: Spectrum of $C_L(t;\tau,\epsilon)$ for $\epsilon = 0.500$; (a) $\tau = 10$, (b) $\tau = 40$, (c) $\tau = 120$, and (d) $\tau = 260$. Amplitude scaled to C_L.

the lift decreases). For larger values of τ, the spectrum becomes more regular; that is, the cascade contains commensurate subharmonics. An example of this is shown in Figures 11c and d. Furthermore, as the gap is increased, the spectrum becomes more regular, and the energy in the subperiods decreases significantly. Examination of all the spectra, particularly for large τ, did not yield a power law relationship in the spectrum. For midvalues of the period, say between $\tau = 30$ and $\tau = 100$, the spectra is more complex: not only are subharmonics present and large, but other degrees of freedom can be seen in the spectra. In fact the half-period component seen in Figure 11b is smaller

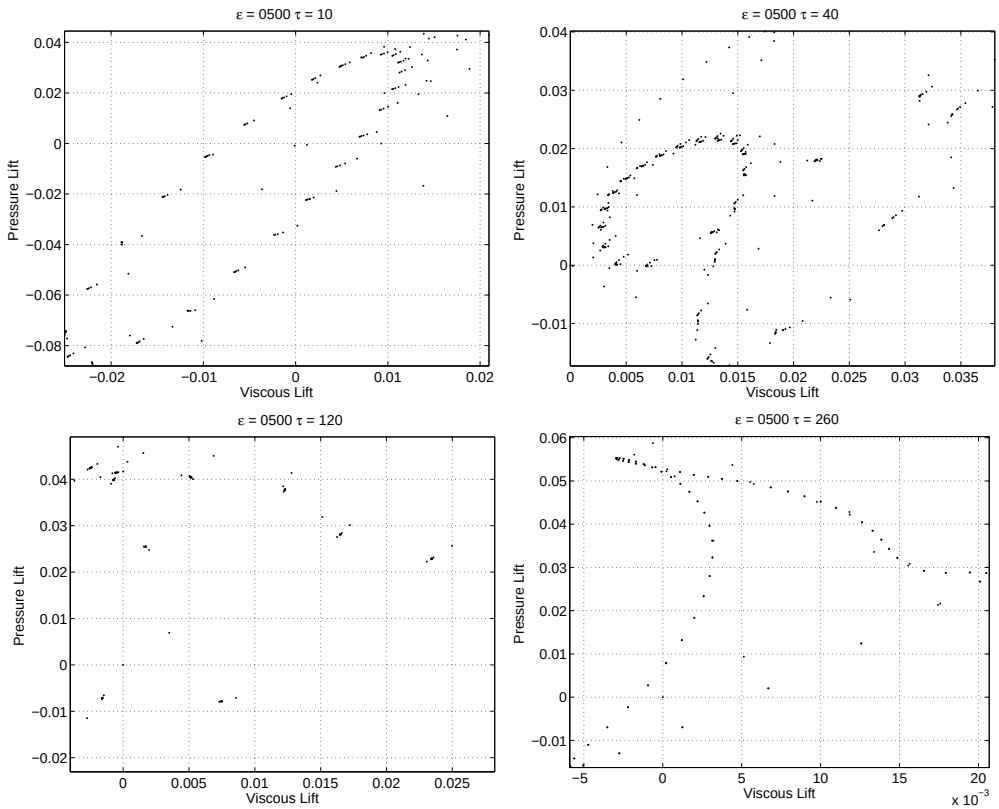

Figure 12: Phase relationship between the pressure and viscous components of the average lift C_{L_A}, for $\epsilon = 0.5$; (a) $\tau = 10$, (b) $\tau = 40$, (c) $\tau = 120$, and (d) $\tau = 260$. Shown here is the superposition of 6.5 periods of data, including the initial transient data.

than other spectral components for the $\tau = 40$ case.

Figure 6 shows that the phase between the viscous and the pressure components of the lift is not constant across all τ. For small values of τ the two components are largely in phase, and the two components play nearly equally important roles in determining the lift. In the transitional region, however, the two components exhibit complex phase relationships and comparable magnitudes. For longer periods the magnitude of both components

falls dramatically, the pressure component dominates, and the phase is still fairly complex. This situation is illustrated in Figure 12, where the points represent values of the components of the lift/drag at different times. The trajectory direction is clockwise for advancing time, except for Figure 12b, which incidentally, corresponds to a case in the transitional range. Figure 12a corresponds to $\epsilon = 0.5$ and $\tau = 10$. For the same gap and $\tau = 40$, Figure 12b shows that the trajectory is a distorted "figure 8." The rightmost portion of the 8 is progressing clockwise. With larger τ, the figure 8 settles to a shape similar to that shown in Figure 12c, the $\tau = 260$ case. Of note is how quickly the pressure component of the lift grows and drops in all cases. In these figures a few spurious points correspond to the early times of the simulation, when transients are present.

5 Combined Lift and Drag

We examine next the combined action of the lift and drag forces and relate certain features of these forces to qualitative changes in the vorticity field. To do so, we have computed force phase diagrams. In contrast to Figure 12, however, these phase diagrams plot the history of the lift against the drag. The phase diagrams are plotted as histories, time being quoted in fractions of the period. In addition, we display the velocity and the magnitude of the vorticity at the associated stages during the cycle. Since the forces are periodic, we display the magnitude of the vorticity only for times after one half-period has transpired.

For $\epsilon = 0.5$ and $\tau = 40$, we see in Figure 13 that the maximum lift is attained when the far field velocity magnitude is near zero. The ascent in

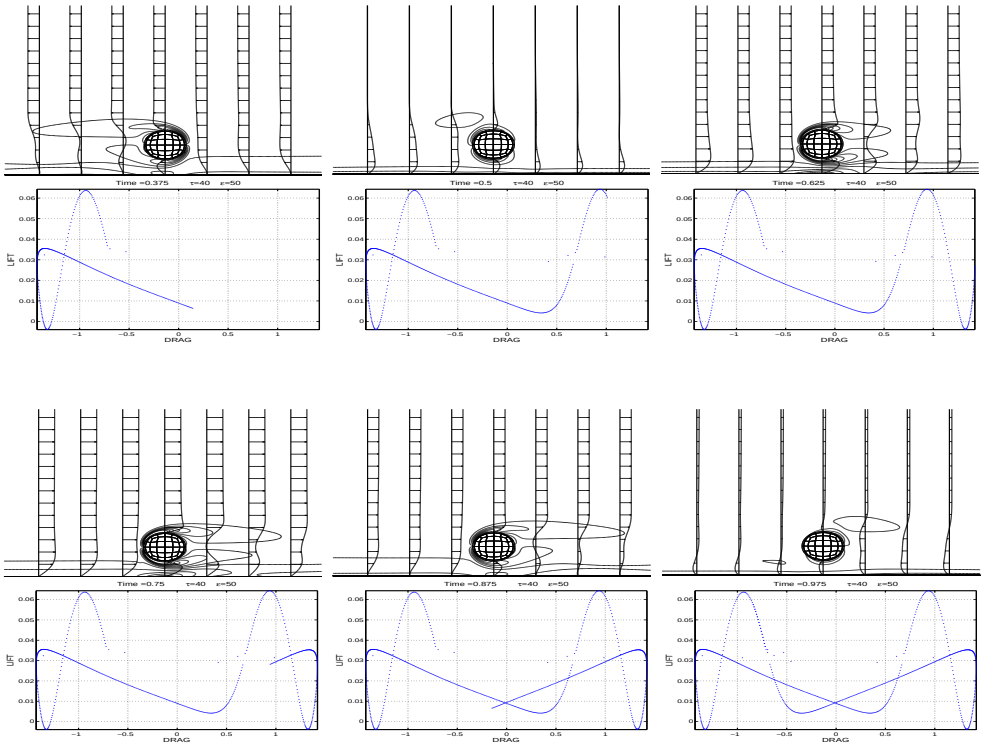

Figure 13: Vorticity magnitude, velocity profiles, and phase portrait at t/τ= .375, .500, .625, .750, .875, and .975 for $\epsilon = 0.5$, $\tau = 40$.

phase space, from the second smallest value of the lift to the largest, occurs very quickly. As the velocity magnitude increases the drag increases further, the lift quickly reaches its minimal value and is then driven slowly to the maximum drag point. Later, as the asymmetry in the vorticity increases, both the drag and the lift decrease. The climb to the maximum value of the lift, following the second smallest value of the lift, is characterized by a considerable amount of vorticity in the neighborhood of the bounding wall.

In Figure 14 we see that the magnitude of the lift in the $\epsilon = 1$ $\tau = 40$ case is smaller than in the $\epsilon = 0.5$ $\tau = 40$ case. We also see that the lift is small in comparison to the drag. In this instance, the lift has only one

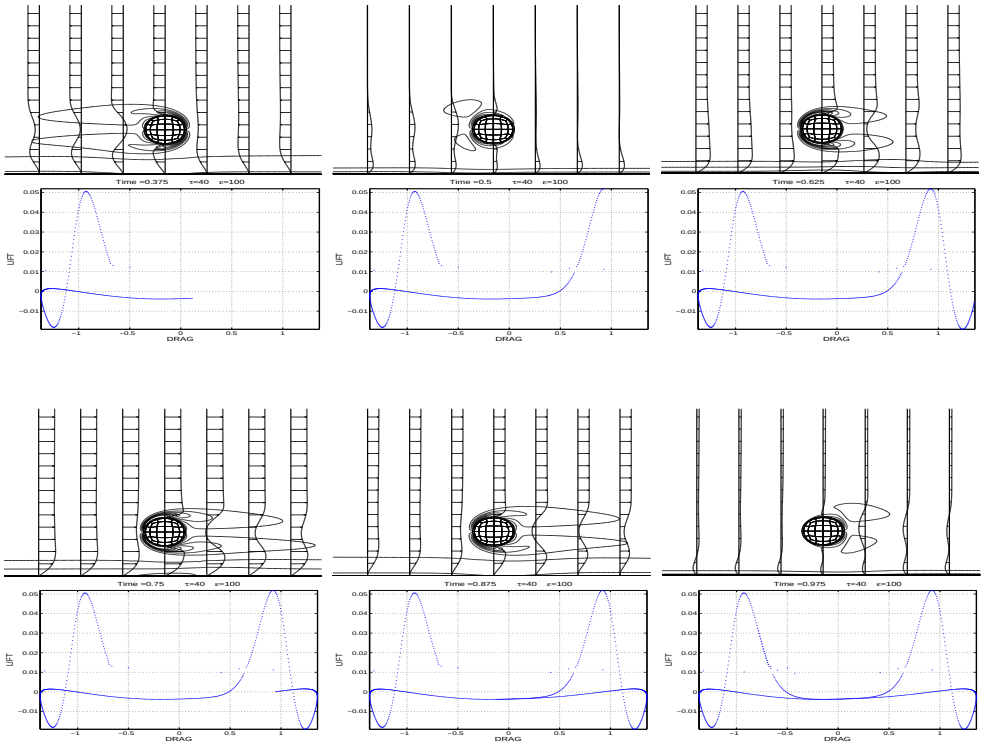

Figure 14: Vorticity magnitude, velocity profiles, and phase portrait at t/τ= .375, .500, .625, .750, .875, and .975 for $\epsilon = 1.0$, $\tau = 40$.

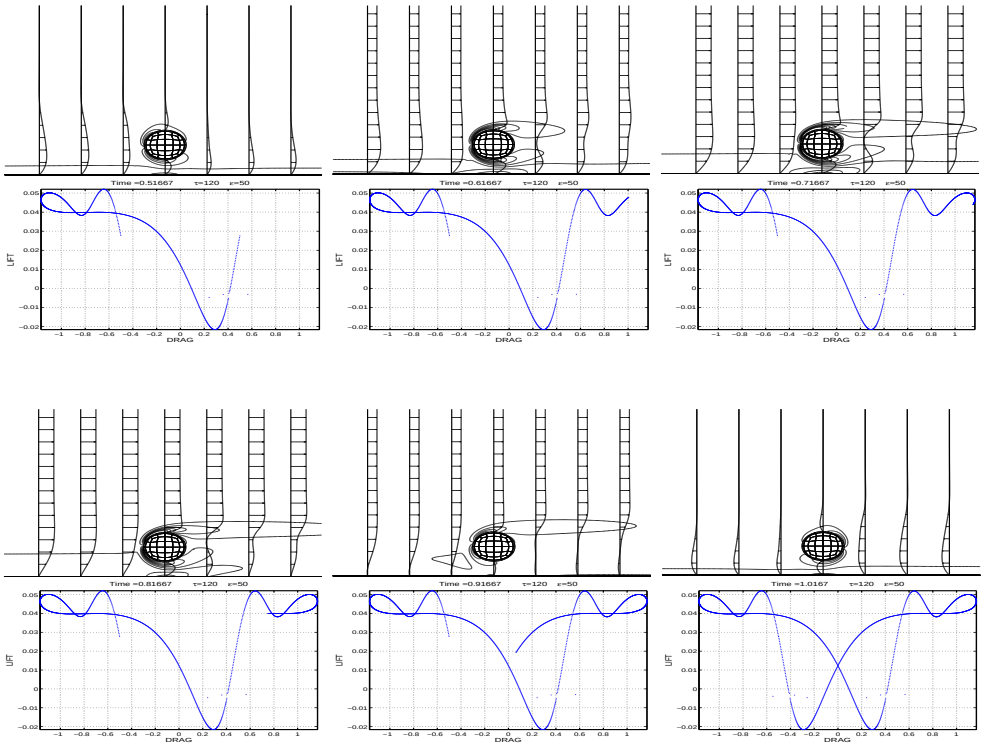

Figure 15: Vorticity magnitude, velocity profiles, and phase portrait at t/τ= .500, .600, .700, .800, .900, and 1.000 for $\epsilon = 0.5$, $\tau = 120$.

minimum and one maximum. The lift maximum coincides with an increase in the asymmetry in the vorticity distribution. This case, as well as that of Figure 13, belongs to the viscous-dominated average-lift regime.

Figure 15 shows the phase portrait and velocity/vorticity distributions for the $\epsilon = 0.5$ and $\tau = 120$ case. In contrast to the preceding cases, it corresponds to a pressure-dominated-regime case. Of note is the appearance of two maxima in the lift and one minimum. We observe, as well, that the time progression of the changes in the lift and drag as a function of time occur more smoothly than in the $\tau = 40$ case. We also note that the lift/drag magnitude ratio of this case is similar to the $\epsilon = 1.0$, $\tau = 40$ case. The main

characteristic that makes this case different from the viscous-dominated cases is the proportion of time the lift is of one sign (in this case positive).

We can relate the spectral analysis of the lift, some of which appears in Figure 11, to the phase plots. Doing so, we reach the following general conclusions: over a full period of the forcing, the two largest maxima and minima in the lift are correlated in time with the largest spectral components. The smaller features are correlated to the smaller amplitude spectral components as well. Since the phase portraits are periodic, with period equal to half the forcing period, the periods of the spectral components smaller than the dominant one must be additively commensurate in smaller groups, usually two. In the transition regime, where the largest spectral component is not the half-period of the forcing, the largest extremum is associated with the largest component of the spectrum, the half-period component with the next largest component. Qualitatively, for moderate ϵ and the larger-τ range, the lift is characterized by a smaller but more sustained positive lift. For the same ϵ, and τ in the transitional range, the lift is characterized by more peaked and shorter-lived bursts. One may speculate that this difference in behavior, when comparing the transitional and the larger-τ regimes, may be associated in an idealized fluid flow as follows: supposing that the buoyancy and lift forces on a particle are comparable in this idealized flow, the transitional regime would be more effective in dislodgement and the longer period regime more effective in keeping a particle in suspension.

6 Summary

In Fischer et al (2002) we numerically computed the lift and drag on a stationary sphere in the neighborhood of an ideal wall boundary, subjected to a time-periodic fluid flow. The lift and drag were obtained as a function of the period of external forcing and Reynolds number. Here we explored how the lift and drag forces change as the gap as well as the forcing period parameters are varied.

The drag force is found to be very uniform in character, for a wide range of period and gap values. The drag is the prevalent force, when compared to the lift, if consideration is limited solely to their relative magnitude; nevertheless the complex phase relationship between the lift and drag suggests that in some contexts ignoring one of the components of the total force would yield a poor description of the dynamics of a particle, unless, perhaps, when the buoyancy force is overwhelming.

We found that there are clearly identifiable regimes in which the average lift is primarily described as viscous- or pressure-dominated. We find that the lift has a range in (ϵ, τ) parameter space in which enhancement takes place and that the lift force is qualitatively different when the gap is present, as compared to the situation where the gap is not there.

This study raises several questions, the most important being the following: Why is there a parameter regime of enhanced averaged lift? What is the underlying reason for there being a pressure and viscous dominated regime in the lift?

This study also concludes that one should be able to build a robust and widely applicable model for the combined lift and drag forces on particles sub-

jected to oscillatory flows. To this end this paper provides a fairly complete description of the forces that should be of considerable aid in formulating such a model.

Several authors, among them Rubinov & Keller (1961); Honji & Taneda (1969); Kurose & Komori (1999), and Kim & Choi (2002), have found that the estimate on the lift forces of spheres and cylinders in steady flows can be significantly affected by ignoring torque. In a future study we intend to take up this question in the context of oscillatory flows using similar methods to those used in this work. Later, we will also characterize the lift and drag forces on a freely moving particle and determine if there is a preferential combination of parameters that lead to sustained suspension or particle dislodgement.

The computed data for lift and drag as a function of time, for periods $10 \leq \tau \leq 300$ and gaps $0 \leq \epsilon \leq 1$, is available and may be obtained by contacting the authors.

Acknowledgments: This work was carried out in part at Argonne National Laboratory under the auspices of the Department of Energy under Contract W-31-109-Eng-38. JMR wishes to thank the DEP and the MCS Division at Argonne, as well as the support by DOE through Grant 329080.

References

Asmolov, E. S. & McLaughlin, J. B. 1999 The inertial lift on an oscillating sphere in a linear shear flow. *Int. J. Multiphase Flow*, **25**, pp. 739–751.

Bearman, P.W., Downie, M.J., Graham, J.M.R. & Obajasu, E.

D. 1985 Forces on cylinders in viscous oscillatory flows at low Keulegan-Carpenter numbers. *J. Fluid Mech.*, **154**, pp. 337–356.

Cherukat, P., McLaughlin, J. B. & Graham, A. L. 1994 The inertial lift on a rigid sphere translating in a linear shear-flow field. *Int. J. Multiphase Flow*, **20**, pp. 339–353.

Fischer, P. F. 1997 An overlapping Schwarz method for spectral element solution of the incompressible Navier-Stokes equations. *J. Comp. Phys.*, **133**, pp. 84–101.

Fischer, P. F. Leaf, G. K. & Restrepo, J. M. 2002 Forces on particles in an oscillatory boundary layer. *J. Fluid Mech.*, **468**, pp. 327–347.

Hall, D. 1988 Measurements of the mean force on a particle near a boundary in turbulent flow. *J. Fluid Mech.*, **187**, pp. 451–466.

Honji, H. & Taneda, A. 1969 Unsteady flow past a circular cylinder. *J. Phys. Soc. Japan*, **27**, pp. 1668–1677.

Justesen, P. 1991 A numerical study of oscillating flow around a circular cylinder. *J. Fluid Mech.*, **222**, pp. 157–196.

Kim, D. & Choi, H. 2002 Laminar flow past a sphere rotating in the streamwise direction. *J. Fluid Mech.*, **461**, pp. 365–386.

Kurose, R. & Komori, S. 1999 Drag and lift forces on a rotating sphere. *J. Fluid Mech.*, **384**, pp. 183–206.

Maday, Y., Patera A. T. & Rønquist, E. M. 1990 An operator-integration-factor splitting method for time-dependent problems: Application to incompressible fluid flow. *J. Sci. Comput.*, **5**(4), pp. 310-337.

Obajasu, E. D., E. D., Bearman, P. W. & Graham, J. M. R. 1988 A study of forces, circulation and vortex patterns around a circular cylinder in oscillating flow. *J. Fluid Mech.*, **196**, pp. 467–494.

Rosenthal, G. & Sleath, J. 1986 Measurements of lift in oscillatory flow. *J. Fluid Mech.*, **146**, pp. 449–467.

Rubinov, S. I. & Keller, J. B. 1961 The transverse force on a spinning sphere moving in a viscous fluid. *J. Fluid Mech.* , **11**, pp. 447–459.

Sarpkaya, T. 1986 Force on a circular cylinder in viscous oscillatory flow at low Keulegan-Carpenter numbers. *J. Fluid Mech.*, **165**, pp. 61–71.

List of Figures

List of Tables